Nonlinear Dyn
https://doi.org/10.1007/s11071-024-10005-2

RESEARCH

A generalized Bouc–Wen model for simulating the quasi-static and dynamic shear responses of helical wire rope isolators

Raffaele Capuano · Nicoló Vaiana · Biagio Carboni

Received: 20 February 2024 / Accepted: 9 July 2024

Abstract This research investigates the mechanical behavior of a helical wire rope isolator deforming along its shear direction. In particular, we present the results of an extensive experimental campaign including both quasi-static and dynamic tests. The former provide hysteresis loops characterizing the device quasi-static behavior; the latter, performed by using an electro-mechanical shaker, furnish frequency response curves describing the dynamic behavior of a rigid block supported by the tested device. To simulate such a complex behavior, we adopt a generalized Bouc–Wen model and identify its parameters on the basis of the quasi-static test results. Subsequently, such a model is employed to reproduce the frequency response curves of the isolated rigid block. Since the results of the dynamic tests suggest the presence of rate-dependent hysteresis phenomena in the isolated system, the generalized Bouc–Wen model is enhanced by introducing a linear viscous component. Finally, to substantiate the model validation, the experimental results obtained by applying a series of white noise signals are compared with those obtained numerically to demonstrate the model capability of reproducing the device behavior in non-stationary response conditions.

Keywords Helical wire rope isolator · Generalized Bouc–Wen model · Asymmetric hysteresis loop · Experimental dynamics

R. Capuano · N. Vaiana
Department of Structures for Engineering and Architecture, University of Naples Federico II, Naples, Italy
e-mail: raffaele.capuano@unina.it

N. Vaiana
e-mail: nicolo.vaiana@unina.it

B. Carboni (✉)
Department of Structural and Geotechnical Engineering, Sapienza University of Rome, Rome, Italy
e-mail: biagio.carboni@uniroma1.it

1 Introduction

One of the core principle of the vibration isolation technique is represented by the adoption of flexible energy dissipating devices capable of reducing the effects of support motion. However, when dealing with problems involving shock and vibrations of individual pieces of equipment or components, isolation can be efficiently accomplished by dissipating input energy using rigid but highly energy absorbing systems [18].

A particular type of highly effective energy dissipating devices, typically used in seismic isolation, is represented by the Helical Wire Rope Isolator (HWRI). This metallic device is renowned for its ability to protect sensitive equipment from the damaging effects of shock and vibrations. It comprises two essential components: a stainless steel cable and two retainer bars, crafted from either aluminum alloy or steel, which securely houses the cable.

Their proven efficiency in dissipating input energy makes them suitable for many applications, especially when sensitive equipment or critical components are

Published online: 11 August 2024

involved. This includes industrial and defense equipment, critical machinery [18], electronic systems [35], as well as more delicate items such as museum artifacts [17], hospital equipment [1], HV circuit breakers [2,3], electrical switchboards in naval ships [26], computer servers [31], and experimental equipment such as the one adopted on the International Space Station [32].

Internal and sliding friction between the braided strands represents the primary source of the typical hysteretic behavior exhibited by HWRIs. This behavior arises due to deformation of HWRI along its principal directions, namely axial, roll, and shear [36,46]. Another important issue characterizing the shape of the force-displacement cycles is the geometric nonlinearity involved in the large deflection of the strands [24,25,28,29]. To allow for their practical application in aerospace [30], civil, mechanical, and naval engineering, comprehensive experimental campaigns, involving both quasi-static and dynamic tests, are generally necessary [34,47]. The complex hysteretic behavior can be characterized by symmetric or asymmetric force-displacement hysteresis loops [5,10,16,43]. Furthermore, when nonlinear analyses are required in the design phase to evaluate the effectiveness of these devices, accurate and computationally efficient hysteretic models become essential. This is especially important when the correct design of an isolation system is crucial for the integrity of valuable objects or structural elements behaving like rocking rigid blocks [19,20].

Over the years, several hysteresis models have been proposed in the literature [21]. Among them, we mention the recently formulated Vaiana-Rosati model [42,44,45] since it is capable of simulating a great variety of complex hysteresis loop shapes. At present, the potentialities of such a model have not fully explored yet, especially in nonlinear dynamics. Therefore, in this work, a generalized version of the widely used Bouc–Wen Model (BWM) of hysteresis is employed [9,49].

The BWM represents a rate-independent hysteresis model, having differential nature, that is able to simulate symmetric force-displacement hysteresis loops. It finds application in reproducing the behavior of many hysteretic mechanical systems and materials used in aerospace, civil, mechanical, and naval engineering. Baber and Wen [8] enhanced the model accounting for stiffness and/or strength degradation; subsequently, Baber and Noori [6,7,11] and Foliente et al. [23] introduced the possibility of simulating pinched hysteresis loops. Other modified and generalized versions of such a model were proposed to obtain asymmetric hysteresis loops [18,22,27,33,34,40], describe an inflection point on the loading branches [39], and collect several effects in one extended formulation [4]. Literature reviews, encompassing rate-independent hysteretic models, including the BWM as well as parameter identification techniques, can be found in [37,48].

The Generalized Bouc–Wen Model (GBWM) employed in this work was proposed by Carboni et al. [15] for modeling the nonlinear restoring forces of a vibration control device. The latter relies on the mechanical behavior of short wire ropes subjected to bending and/or tensile cyclic loads. In [15], the authors introduced a new pinching BWM to describe the quasi-static and dynamic responses of this versatile hysteretic tuned mass damper made of steel and NiTiNOL strands. This device can provide hardening or softening behavior depending on the configuration adopted [13,14]. Thus, the model was generalized to simulate the typical asymmetric hysteresis loops exhibited by the proposed hysteretic tuned mass damper due to large excitation and unexpected situation [16]. The capability to accurately reproduce a variety of hysteresis loop shapes enlarged its applicability to composite materials [50] and wire rope isolators [38]. Notably, the GBWM stands out for its effectiveness in capturing both quasi-static and dynamic responses, making it a valuable tool within heuristic algorithms. Its capabilities make it a solid choice for in-depth understanding and simulation of complex hysteretic mechanical behaviors, such as those exhibited by HWRIs.

This study investigates both quasi-static and dynamic responses of a HWRI when it deforms along its shear direction. The complex behavior of the device is simulated using the GBWM and the model parameters are determined based on quasi-static test results. Parameter identification is performed using the differential evolution algorithm to minimize the mean square error between experimental and simulated force-displacement hysteresis loops. In particular, it is verified if the parameters calibrated on the basis of quasi-static tests are representative of the dynamic behavior of the device in stationary and non-stationary conditions.

The paper is organized into four parts. In the first one (Sect. 2), details about the investigated device, with particular reference to its geometry, dimensions and

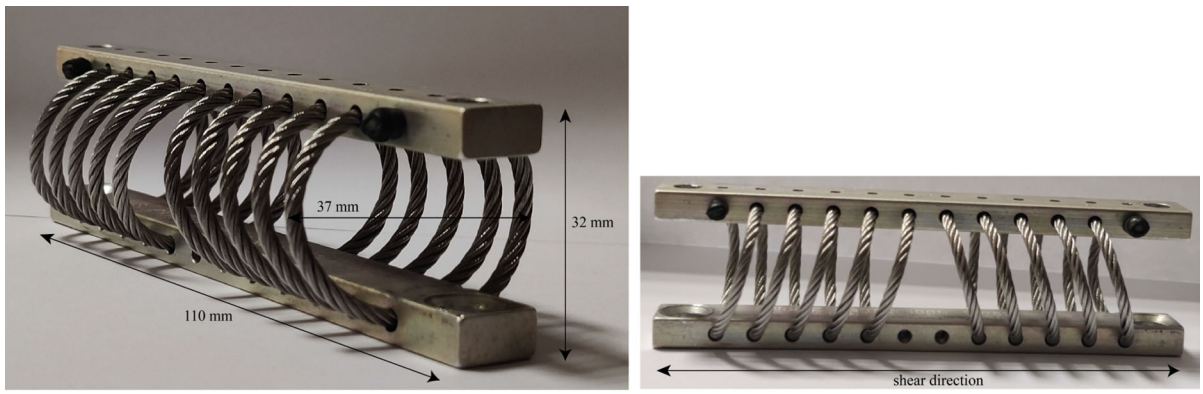

Fig. 1 Helical wire rope isolator: **a** tested device with geometric dimensions and **b** side view showing the shear direction

constituting materials, are illustrated. In addition, the results of quasi-static and dynamic tests are presented and discussed: the former provide the device hysteresis loops whereas the latter the Frequency Response Curves (FRCs) associated with an isolated rigid block subjected to increasing levels of the base excitation. In Sect. 3, the equilibrium equations of the adopted mathematical model are illustrated, with a focus on the derivation of the non-dimensional GBWM. Section 4 describes the procedures employed to identify the model parameters on the basis of the quasi-static test results. Finally, in Sect. 5, the model is employed, with and without an additional linear viscous component, to numerically compute the FRCs obtained for the isolated rigid block as well as to reproduce the experimental displacement histories of the rigid block excited by a series of white noise signals imposed at the base.

2 Helical wire rope isolator: experimental campaigns

Figure 1a shows the tested HWRI that differs from similar devices, already studied in previous works [38,46], because of the arrangement of the stainless steel strands. Indeed, two helically shaped strands, with different angles, are affixed to both the upper and lower steel plates thus producing an asymmetric hysteretic behavior when the device deforms along its shear direction (Fig. 1b), as it will be shown in the sequel.

The selected device is characterized by an overall length of 110 mm and a height of 32 mm. In addition, the ropes exhibit a diameter of 2.2 mm and the helical coils have a width of 37 mm. The above-mentioned asymmetric hysteretic behavior of the tested HWRI is attributed to the variation in winding pitches, with the right (left) coils having a winding pitch of 7 mm (9 mm). Finally, the device mass is equal to 0.065 kg.

The complex behavior exhibited by such a HWRI was experimentally investigated at the Materials and Structures Laboratory of the Sapienza University of Rome (Italy) by performing both quasi-static (Sect. 2.1) and dynamic (Sect. 2.2) tests.

2.1 Quasi-static tests

Quasi-static tests were performed by adopting a Zwick-Roell machine. In particular, increasing displacement ramps, at constant velocity, were applied along the device shear direction and the associated restoring force was measured.

In order to avoid a hardening effect, the relative displacement between the two plates, along the direction orthogonal to the shear one, was left free by placing one of the two plates on a transversal slider. In such a way, when the displacement ramps were applied to one of the plates along the shear direction, they were free to get closer thus preventing the elongation of the strands.

The results of the experimental tests are shown in Fig. 2. In particular, Fig. 2a illustrates the time history of the restoring force whereas Fig. 2b shows the restoring force-displacement hysteresis loops.

Looking at Fig. 2b, we may observe that the hysteresis loops present an asymmetric nature. Indeed, taking the same displacement absolute values along the positive and negative parts of the horizontal axis, different

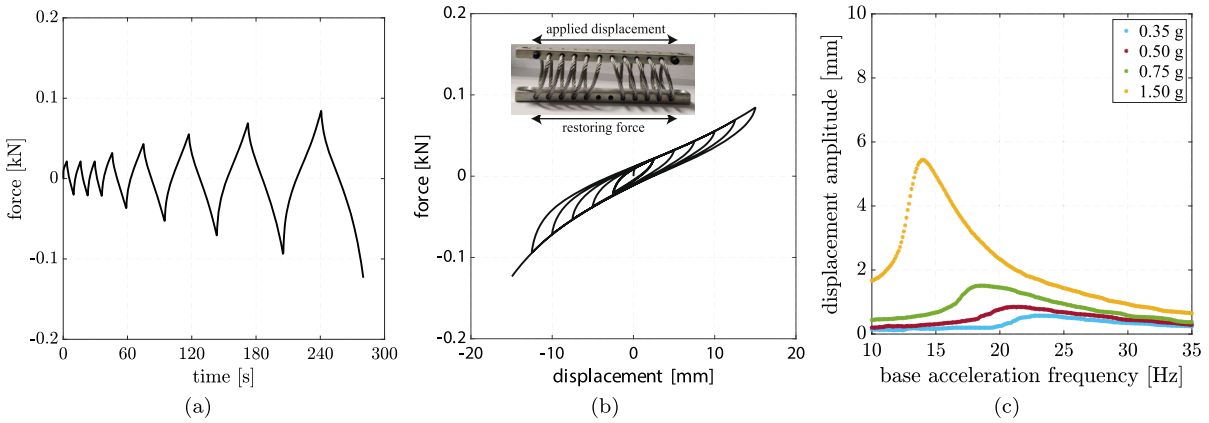

Fig. 2 Experimental results: **a** time history of the restoring force, **b** force-displacement hysteresis loops and **c** frequency response curves

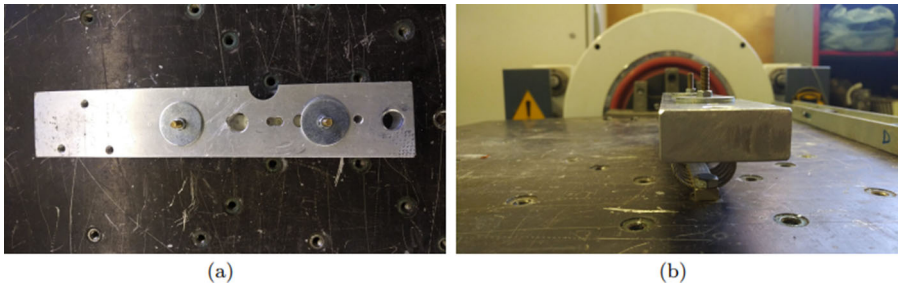

Fig. 3 Experimental setup employed for acquiring the FRCs of the rigid block connected to the shaker slip table by means of the HWRI: **a** top and **b** side views

values of the restoring force are reached along the vertical axis.

Finally, we may note that the hysteresis loops exhibit a softening behavior for small displacements and a hardening behavior as the displacement amplitude increases, with the latter more pronounced in the direction of displacement assumed to be negative. It is quite reasonable to associate the softening behavior with dissipative phenomena due to the friction of the wires and the hardening one with the geometric nonlinearities that become dominant with increasing displacements.

2.2 Dynamic tests

Dynamic tests were carried out by employing a mechanical shaker driven in closed loop by the Simcenter Testlab system. To this end, an aluminum rigid block, having mass of 0.735 kg, including auxiliary bolts, was mounted on the top of the HWRI whereas the latter was connected to the shaker slip table, as shown in Fig. 3.

One PCB accelerometer was attached to the rigid block and another one was placed on the slip table in order to drive and measure the base excitation. A micro-epsilon linear laser was also clamped on the slip table to measure the relative displacement of the rigid block.

Frequency sweep tests were performed in the frequency range [10, 35] Hz with a sweep rate of 0.02 Hz/sec; the rigid block relative displacement amplitude was acquired by means of an harmonic estimator that was set to a resolution of 0.10 Hz.

Figure 2c presents the FRCs obtained for four different values of the base acceleration amplitude, that is, 0.35 g, 0.50 g, 0.75 g and 1.50 g where g indicates the gravity acceleration. Such FRCs show a marked softening behavior considering that the resonance frequency decreases from approximately 23 Hz, in the curve obtained for an acceleration amplitude of 0.35 g, to 13 Hz, in the curve acquired for an acceleration amplitude of 1.50 g. The resonance displacement amplitudes, associated with such two curves, assume values of approximately 0.50 mm and 5.50 mm, respectively. This behavior is in complete agreement with the hysteresis loops illustrated in Fig. 2b, considering that,

within this range of displacement, the softening behavior is clearly discernible.

3 Mathematical model

In this section we present the mathematical model adopted to perform the numerical simulations. In particular, we first derive the dimensional equilibrium equation of a Single Degree of Freedom (SDoF) hysteretic mechanical system and present the adopted GBWM (Sect. 3.1). Subsequently, we perform the non-dimensionalization of both the equilibrium equation (Sect. 3.2) and the hysteresis model (Sect. 3.3). The latter are particularly useful to improve the computational efficiency of the algorithms adopted to perform the numerical simulations presented in Sects. 4 and 5.

3.1 Dimensional equilibrium equation

The selected SDoF hysteretic mechanical system consists of a mass m connected to two different types of elements:

- a rate-dependent hysteretic element;
- a rate-independent hysteretic element.

Denoting by u, $\dot{u}$ and $\ddot{u}$ the generalized displacement, velocity and acceleration of the mass, respectively, the dimensional equilibrium equation of the system can be derived from the general form of the Newton's second law as:

$$m\ddot{u} + f_{rd}(\dot{u}) + f_{ri}(u) = p\,(t)\,, \tag{1}$$

where f_{rd} and f_{ri} represent the generalized rate-dependent and rate-independent hysteretic forces, respectively, exerted on the related hysteretic element, whereas p is the generalized external force that is a function of time t.

In this paper, the generalized rate-independent hysteretic force f_{ri} is evaluated by using the GBWM proposed by Carboni et al. [16]. Such a model is versatile and can accurately simulate a number of different hysteresis loop shapes. Additionally, it proves to be effective when used in heuristic algorithms for the identification of both quasi-static and dynamic responses.

According to the GBWM, f_{ri} is computed as the sum of three components:

$$f_{ri}(u) = f_e(u) + f_c(u) + z(u), \tag{2}$$

where f_e (f_c) represents a linear (nonlinear) elastic force whereas z is a rate-independent hysteretic force.

In particular, the expression of f_e is:

$$f_e(u) = k_e u, \tag{3}$$

whereas the one of f_c is:

$$\begin{aligned} f_c(u) = {} & k_3 u^3 + H^+ k_3^+ \left(u - u_0^+\right)^3 + \\ & H^- k_3^- \left(|u| - u_0^-\right)^3. \end{aligned} \tag{4}$$

We note that the second (third) term of the previous equation is a function acting when the threshold displacement u_0^+ ($-u_0^-$) is reached. In addition, H^+ and H^- are defined as follows:

$$\begin{aligned} H^+ &= \frac{+1 + \operatorname{sgn}\left(u - u_0^+\right)}{2}, \\ H^- &= \frac{-1 + \operatorname{sgn}\left(u + u_0^-\right)}{2}. \end{aligned} \tag{5}$$

As far as z is concerned, it is evaluated by solving the following first order ordinary differential equation:

$$\dot{z} = \left\{k_d h + k_d^+ h^+ + k_d^- h^- - [\gamma + \beta \operatorname{sgn}(z\dot{u})]|z|^n\right\}\dot{u}, \tag{6}$$

in which h, h^+ and h^- are pinching functions having expressions:

$$\begin{aligned} h(u) &= 1 - \xi e^{-\frac{u^2}{u_c}}, \\ h^+(u) &= 1 - e^{-\frac{\left(|u| - u_b^+\right)^2}{u_c^+} L^+ L_v^+}, \\ h^-(u) &= 1 - e^{-\frac{\left(|u| - u_b^-\right)^2}{u_c^-} L^- L_v^-}, \end{aligned} \tag{7}$$

with:

$$L^+ = \frac{1+\text{sgn}\left(u-u_b^+\right)}{2}, \quad L_v^+ = \frac{1+\text{sgn}(\dot{u})}{2}, \\ L^- = \frac{1-\text{sgn}\left(u+u_b^-\right)}{2}, \quad L_v^- = \frac{1-\text{sgn}(\dot{u})}{2}. \tag{8}$$

We may observe that the terms $k_d^+ h^+$ and $k_d^- h^-$ act exclusively when the threshold displacements u_b^+ and $-u_b^-$ are respectively reached.

Finally, the quantities k_e, k_3, k_3^+, k_3^-, u_0^+, u_0^-, k_d, k_d^+, k_d^-, γ, β, n, ξ, u_c, u_c^+, u_c^-, u_b^+, u_b^- represent the eighteen model parameters that need to be calibrated from experimental tests. The conditions that need to be satisfied by such parameters can be found in [16].

3.2 Non-dimensional equilibrium equation

The adopted non-dimensionalization procedure consists of five distinct steps [12] that are briefly illustrated, in the sequel, for the reader's convenience:

i) *variables identification*: identify all the independent and dependent variables appearing in the equation to be non-dimensionalized;
ii) *non-dimensional variables introduction*: replace such variables with non-dimensional counterparts obtained by introducing characteristic units;
iii) *equation normalization*: normalize the resulting equation dividing it by the coefficient of the highest order term;
iv) *characteristic units selection*: assign expressions to the characteristic units thus obtaining simple auxiliary conditions;
v) *expression in non-dimensional form*: reformulate the equation in terms of the identified non-dimensional parameters.

Let us apply the above-illustrated five steps to Eq. (1) governing the dynamic behavior of the analyzed system.

i) We observe that time t is the independent variable whereas both the generalized displacement u and rate-independent hysteretic force z represent the dependent ones.
ii) We introduce the corresponding non-dimensional variables:

$$\tau := \frac{t}{t_s}, \quad x := \frac{u}{u_s}, \quad \rho := \frac{z}{z_s}, \tag{9}$$

in which t_s, u_s and z_s represent the characteristic units that, in such a case, assume the role of dimensional scaling factors. Consequently, the dimensional variables can be expressed as follows:

$$t = t_s \tau, \quad u = u_s x, \quad z = z_s \rho. \tag{10}$$

On the basis of Eq. (10), Eq. (1) becomes:

$$\frac{m u_s}{t_s^2}\ddot{x} + f_{rd}\left(\frac{u_s}{t_s}\dot{x}\right) + z_s \tilde{f}_{ri}(x) = p\left(t_s \tau\right), \tag{11}$$

in which an overdot represents differentiation with respect to the non-dimensional time τ, whereas $\tilde{f}_{ri}$ is the non-dimensional rate-independent hysteretic force defined as:

$$\tilde{f}_{ri}(x) = \tilde{f}_e(x) + \tilde{f}_c(x) + \rho(x). \tag{12}$$

In particular, as a consequence of the non-dimensional variables substitution, the non-dimensional linear elastic force $\tilde{f}_e$ is:

$$\tilde{f}_e(x) := \frac{f_e(u_s x)}{z_s} = \frac{k_e u_s}{z_s} x, \tag{13}$$

whereas, the non-dimensional nonlinear elastic force $\tilde{f}_c$ is:

$$\tilde{f}_c(x) := \frac{f_c(u_s x)}{z_s} = \frac{k_3 u_s^3}{z_s} x^3 + \\ + \tilde{H}^+ \frac{k_3^+}{z_s}\left(u_s x - u_0^+\right)^3 + \\ + \tilde{H}^- \frac{k_3^-}{z_s}\left(|u_s x| - u_0^-\right)^3, \tag{14}$$

with:

$$\tilde{H}^+ = \frac{+1+\text{sgn}\left(u_s x - u_0^+\right)}{2}, \\ \tilde{H}^- = \frac{-1+\text{sgn}\left(u_s x + u_0^-\right)}{2}. \tag{15}$$

Finally, the rate equation defining the non-dimensional rate-independent hysteretic force ρ becomes:

$$\frac{z_s}{t_s}\dot{\rho} = \left\{k_d\tilde{h} + k_d^+\tilde{h}^+ + k_d^-\tilde{h}^- + \right.$$
$$\left. - \left[\gamma + \beta\,\mathrm{sgn}\left(\frac{z_s u_s}{t_s}\rho\dot{x}\right)\right]|z_s\rho|^n\right\}\frac{u_s}{t_s}\dot{x}, \tag{16}$$

in which $\tilde{h}$, $\tilde{h}^+$ and $\tilde{h}^-$ are defined as:

$$\begin{aligned}
\tilde{h}(x) &= 1 - \xi e^{-\frac{(u_s x)^2}{u_c}},\\
\tilde{h}^+(x) &= 1 - e^{-\frac{\left(|u_s x| - u_b^+\right)^2}{u_c^+}\tilde{L}^+\tilde{L}_v^+},\\
\tilde{h}^-(x) &= 1 - e^{-\frac{\left(|u_s x| - u_b^-\right)^2}{u_c^-}\tilde{L}^-\tilde{L}_v^-},
\end{aligned} \tag{17}$$

with:

$$\begin{aligned}
\tilde{L}^+ &= \frac{1 + \mathrm{sgn}\left(u_s x - u_b^+\right)}{2},\\
\tilde{L}_v^+ &= \frac{1 + \mathrm{sgn}\left(\frac{u_s}{t_s}\dot{x}\right)}{2},\\
\tilde{L}^- &= \frac{1 - \mathrm{sgn}\left(u_s x + u_b^-\right)}{2},\\
\tilde{L}_v^- &= \frac{1 - \mathrm{sgn}\left(\frac{u_s}{t_s}\dot{x}\right)}{2}.
\end{aligned} \tag{18}$$

iii) We note that, in Eqs. (11) and (16), the coefficients of the highest order term are $\frac{mu_s}{t_s^2}$ and $\frac{z_s}{t_s}$, respectively. Hence, upon dividing Eq. (11) by $\frac{mu_s}{t_s^2}$ as well as Eq. (16) by $\frac{z_s}{t_s}$, we obtain:

$$\ddot{x} + \frac{t_s^2}{mu_s} f_{rd}\left(\frac{u_s}{t_s}\dot{x}\right) + \frac{z_s t_s^2}{mu_s}\tilde{f}_{ri}(x) = \frac{t_s^2}{mu_s} p\left(t_s\tau\right), \tag{19}$$

and

$$\dot{\rho} = \frac{u_s}{z_s}\left\{k_d\tilde{h} + k_d^+\tilde{h}^+ + k_d^-\tilde{h}^- + \right.$$
$$\left. - \left[\gamma + \beta\,\mathrm{sgn}\left(\frac{z_s u_s}{t_s}\rho\dot{x}\right)\right]|z_s\rho|^n\right\}\dot{x}. \tag{20}$$

iv) To simplify the dimensionless expressions, we set:

$$t_s^2 := \frac{mu_c}{\sqrt[n]{\frac{k_d + k_d^+ + k_d^-}{\gamma + \beta}}},$$
$$u_s := u_c,$$
$$z_s := \sqrt[n]{\frac{k_d + k_d^+ + k_d^-}{\gamma + \beta}}, \tag{21}$$

thus obtaining the following auxiliary condition:

$$\frac{z_s t_s^2}{mu_s} = 1. \tag{22}$$

v) We finally provide the non-dimensional equilibrium equation:

$$\ddot{x} + \frac{f_{rd}\left(\frac{u_s}{t_s}\dot{x}\right)}{z_s} + \tilde{f}_{ri}(x) = \frac{p\left(t_s\tau\right)}{z_s}, \tag{23}$$

that can be rewritten as:

$$\ddot{x} + \tilde{f}_{rd}(\dot{x}) + \tilde{f}_{ri}(x) = \tilde{p}\left(\tau\right), \tag{24}$$

after defining:

$$\tilde{f}_{rd}(\dot{x}) := \frac{f_{rd}\left(\frac{u_s}{t_s}\dot{x}\right)}{z_s}, \quad \tilde{p}\left(\tau\right) := \frac{p\left(t_s\tau\right)}{z_s}. \tag{25}$$

3.3 Non-dimensional hysteresis model

To derive the Non-Dimensional Generalized Bouc–Wen Model (NDGBWM), we first introduce the following non-dimensional parameters:

$$\begin{aligned}
&\tilde{k}_e := \frac{k_e u_s}{z_s},\\
&\tilde{k}_3 := \frac{k_3 u_s^3}{z_s}, \quad \tilde{k}_3^+ := \frac{k_3^+ u_s^3}{z_s}, \quad \tilde{k}_3^- := \frac{k_3^- u_s^3}{z_s},\\
&\tilde{k}_d := \frac{k_d u_s}{z_s}, \quad \tilde{k}_d^+ := \frac{k_d^+ u_s}{z_s}, \quad \tilde{k}_d^- := \frac{k_d^- u_s}{z_s},\\
&x_c := \frac{u_c}{u_s^2}, \quad x_c^+ := \frac{u_c^+}{u_s^2}, \quad x_c^- := \frac{u_c^-}{u_s^2},\\
&x_0^+ := \frac{u_0^+}{u_s}, \quad x_0^- := \frac{u_0^-}{u_s},\\
&x_b^+ := \frac{u_b^+}{u_s}, \quad x_b^- := \frac{u_b^-}{u_s},\\
&\tilde{\gamma} := \gamma u_s\,|z_s|^{n-1},\\
&\tilde{\beta} := \beta u_s\,|z_s|^{n-1}.
\end{aligned} \tag{26}$$

Table 1 GBWM parameters adopted for simulating the responses in Fig. 4

k_e	k_3^+	k_3^-	k_d	k_d^-	γ	β	n
[kN/mm]	$[\text{kN/mm}^3]$	$[\text{kN/mm}^3]$	[kN/mm]	[kN/mm]	[1/mm]	[1/mm]	[−]
4.614×10^{-3}	5.377×10^{-7}	8.981×10^{-6}	1.173×10^{-2}	8.758×10^{-2}	0.584	0.584	1

Consequently, the non-dimensional linear elastic force $\tilde{f}_e$, given in Eq. (13), becomes:

$$\tilde{f}_e(x) = \tilde{k}_e x, \tag{27}$$

whereas the non-dimensional nonlinear elastic force, provided by Eq. (14), is rewritten as:

$$\begin{aligned} \tilde{f}_c(x) = & \tilde{k}_3 x^3 + \\ & + \tilde{H}^+ \tilde{k}_3^+ \left(x - x_0^+\right)^3 + \\ & + \tilde{H}^- \tilde{k}_3^- \left(|x| - x_0^-\right)^3, \end{aligned} \tag{28}$$

with:

$$\begin{aligned} \tilde{H}^+ &= \frac{+1 + \text{sgn}\left(x - x_0^+\right)}{2}, \\ \tilde{H}^- &= \frac{-1 + \text{sgn}\left(x + x_0^-\right)}{2}. \end{aligned} \tag{29}$$

Finally, the non-dimensional first order ordinary differential equation in (20), that allows for the evaluation of the non-dimensional rate-independent hysteretic force $\rho(u)$, becomes:

$$\begin{aligned} \dot{\rho} = & \left\{ \tilde{k}_d \tilde{h} + \tilde{k}_d^+ \tilde{h}^+ + \tilde{k}_d^- \tilde{h}^- + \right. \\ & \left. - \left[\tilde{\gamma} + \tilde{\beta}\, \text{sgn}(\rho \dot{x}) \right] |\rho|^n \right\} \dot{x}, \end{aligned} \tag{30}$$

in which $\tilde{h}$, $\tilde{h}^+$ and $\tilde{h}^-$ are defined as:

$$\begin{aligned} \tilde{h}(x) &= 1 - \xi e^{-\frac{x^2}{x_c}}, \\ \tilde{h}^+(x) &= 1 - e^{-\frac{\left(|x| - x_b^+\right)^2}{x_c^+} \tilde{L}^+ \tilde{L}_v^+}, \\ \tilde{h}^-(x) &= 1 - e^{-\frac{\left(|x| - x_b^-\right)^2}{x_c^-} \tilde{L}^- \tilde{L}_v^-}, \end{aligned} \tag{31}$$

with:

$$\begin{aligned} \tilde{L}^+ &= \frac{1 + \text{sgn}\left(x - x_b^+\right)}{2}, \quad \tilde{L}_v^+ = \frac{1 + \text{sgn}(\dot{x})}{2}, \\ \tilde{L}^- &= \frac{1 - \text{sgn}\left(x + x_b^-\right)}{2}, \quad \tilde{L}_v^- = \frac{1 - \text{sgn}(\dot{x})}{2}. \end{aligned} \tag{32}$$

4 Simulation of quasi-static response

In the sequel, we employ the GBWM, presented in Sect. 3.1, to reproduce the complex experimental behavior exhibited by the tested HWRI and illustrated in Fig. 2a, in terms of restoring force history, as well as in Fig. 2b, in terms of force-displacement hysteresis loops.

In particular, the optimal model parameters are identified by minimizing the Mean Square Error (MSE) defined as:

$$\text{MSE}(\mathbf{p}) = \frac{100}{N \sigma_{\mathbf{f}_e}} \sum_{j=1}^{N} \left[f_{exp}(u_j, t_j) - f_s(u_j, t_j, \mathbf{p}) \right]^2, \tag{33}$$

where N represents the number of time instants t_j at which the experimental restoring force $f_{exp}(u_j, t_j)$ and the applied displacement u_j are recorded (e.g., $t_0 = 0$ and $t_N = T$), whereas $\sigma_{\mathbf{f}_e}$ is the variance of the experimentally acquired restoring force vector. In addition, the term $f_s(u_j, t_j, \mathbf{p})$ indicates the simulated restoring force at the time instant t_j, evaluated according to the tentative values of the parameters collected in vector $\mathbf{p}$.

The parameter identification is conducted by means of the Differential Evolution (DE) algorithm [15,41] by adopting 200 vectors for each population, normally distributed on the research space, and performing 1000 iterations. The mutation coefficient is set equal to 0.9 whereas the crossing probability equal to 0.5.

The identified model parameters, obtained with a MSE of 0.21%, are presented in Table 1. We note that

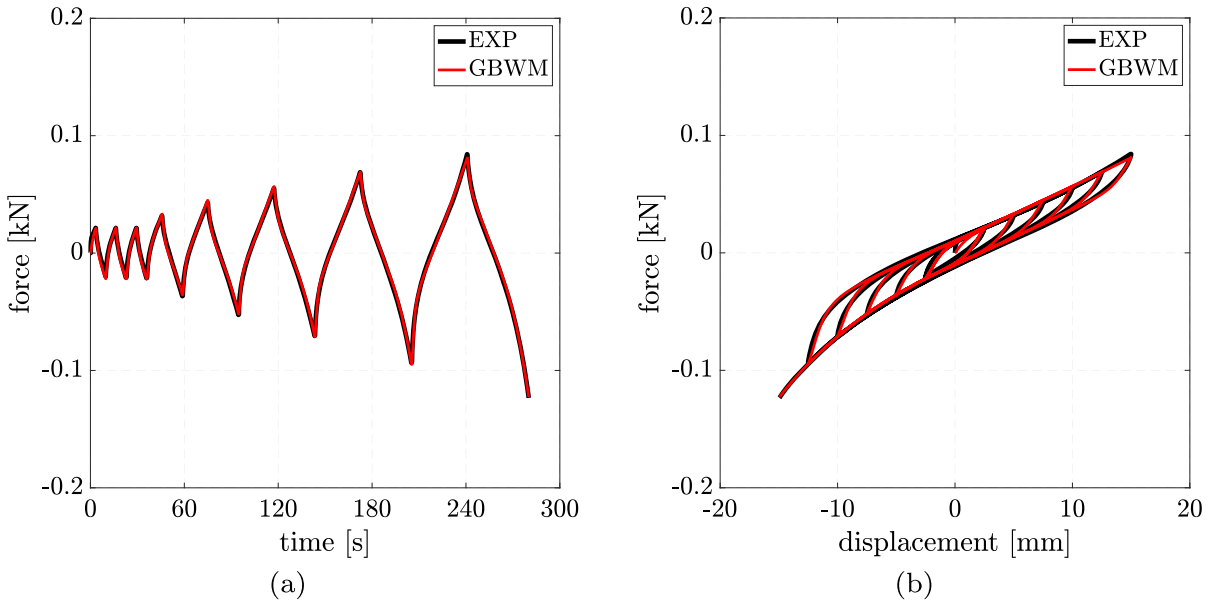

Fig. 4 Experimental versus simulated responses obtained by using the GBWM parameters in Table 1: **a** time history of the restoring force and **b** force-displacement hysteresis loops

Table 2 NDGBWM parameters adopted for simulating the responses in Fig. 5

$\tilde{k}_e$	$\tilde{k}_3^+$	$\tilde{k}_3^-$	$\tilde{k}_d$	$\tilde{k}_d^-$	$\tilde{\gamma}$	$\tilde{\beta}$	n
[−]	[−]	[−]	[−]	[−]	[−]	[−]	[−]
54.266	6.324×10^3	1.056×10^5	137.958	1.030×10^3	584	584	1

$u_c = u_c^+ = u_c^- = 1000$ whereas all the other parameters, not listed in the table, are set equal to zero, and the function $\tilde{L}_v^-$ is equal to 1.

In addition, to clearly show the model accuracy, Fig. 4a compares the experimental and simulated restoring force histories whereas Fig. 4b presents a comparison between the experimental and simulated force-displacement hysteresis loops.

The identified dimensional parameters, given in Table 1, are subsequently used to derive the corresponding non-dimensional ones, listed in Table 2, by adopting Eq. (26).

For the reader's convenience, Fig. 5 presents the force-displacement relations associated with the three terms defined in Eq. (12) and computed by employing the parameters in Table 2.

It is crucial to note that, although the results illustrated in Sects. 4 and 5 are presented in terms of the GBWM, the MATLAB codes, employed to perform the simulations, adopt the NDGBWM for computational efficiency reasons.

5 Simulation of dynamic response

In this section, the mathematical model illustrated in Sect. 3.1 is employed to simulate the complex experimental dynamic response of the isolated rigid block in both stationary (Sect. 5.1) and non-stationary (Sect. 5.2) conditions.

In particular, it is shown that, for accuracy reasons, it may be necessary not only to adopt the GBWM, whose parameters are identified by using the quasi-static test results, but also a linear rate-dependent hysteresis model able to take into account rate-dependent hysteresis phenomena observed in dynamic tests.

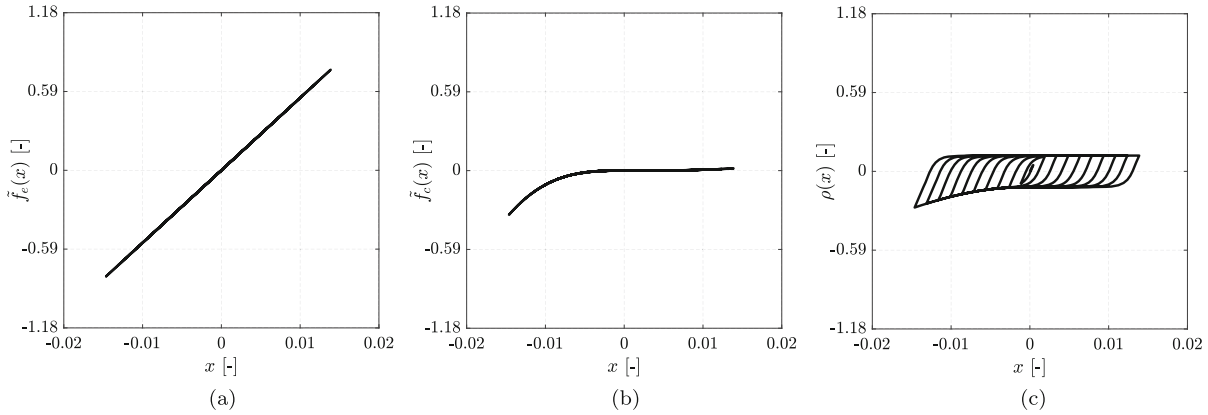

Fig. 5 Force-displacement relations simulated by using the NDGBWM parameters in Table 2: **a** non-dimensional linear elastic force, **b** nonlinear elastic force and **c** rate-independent hysteretic force

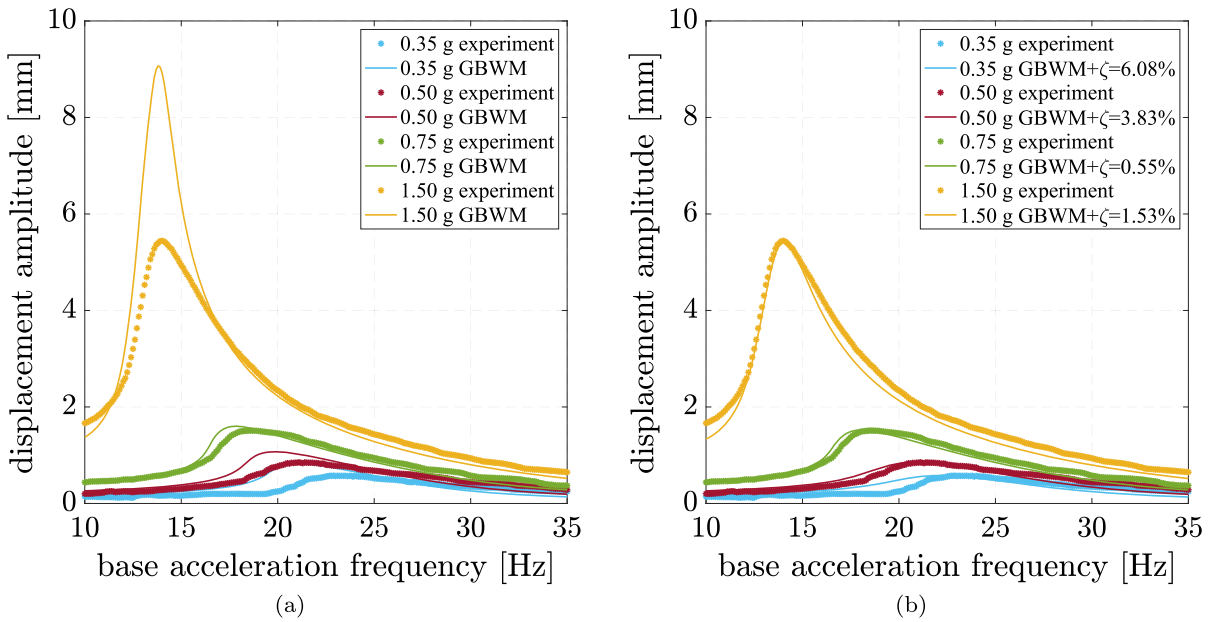

Fig. 6 Comparison between experimental FRCs and those simulated by using the **a** GBWM as well as the **b** GBWM with additional linear viscous damping

5.1 Stationary response

In the sequel, we investigate the capability of the GBWM, calibrated on the basis of the quasi-static tests, to simulate the FRCs, illustrated in Fig. 2c, obtained by imposing harmonic accelerations at the base of the isolated rigid block.

To this end, the mathematical model described in Sect. 3.1 is employed. In particular, the mass m is assumed to be the sum of the rigid block mass (0.7350 kg) and half of the device mass (0.0325 kg) whereas the adopted GBWM parameters are those listed in Table 1.

To numerically evaluate the FRCs, the MATLAB ode45 function is employed and a frequency step of 0.10 Hz is used within the range [10, 35] Hz. In addition, as done in the experimental tests, the FRCs are obtained for four different values of base acceleration amplitude, that is, 0.35 g, 0.50 g, 0.75 g, 1.50 g.

The comparison between experimental and simulated FRCs, shown in Fig. 6a, reveals crucial pieces of

information on the complex dynamics of the analyzed mechanical system. Indeed, it can be noted that, for base acceleration amplitudes equal to 0.35 g, 0.50 g and 1.50 g, the adopted mathematical model overestimates the mass relative displacement amplitudes in the region close to the resonance frequency. On the other hand, for the base acceleration amplitude of 0.75 g, a moderate overestimation is observed. Such a discrepancy is more likely to be associated with additional damping phenomena, having rate-dependent nature, that are not present in the performed quasi-static tests adopted to calibrate the GBWM parameters.

Accordingly, to drastically improve the accuracy of the numerical simulations, the mathematical model is enriched by using a linear rate-dependent hysteretic element. In particular, for each FRC, an equivalent damping ratio ζ, associated with the linear resonance frequency computed as $\sqrt{k_e/m}$, with k_e provided by Table 1, is evaluated to minimize the MSE_s defined as:

$$\mathrm{MSE}_s(\zeta) = \frac{100}{N\sigma_{\mathbf{A}_e}} \sum_{j=1}^{N} \left[A_{exp}(f_j) - A_s(f_j, \zeta)\right]^2. \tag{34}$$

In such a case, N represents the number of stationary displacement amplitudes $A_{exp}(f_j)$ experimentally acquired at the base acceleration frequency f_j whereas $\sigma_{\mathbf{A}_e}$ indicates the variance of the displacement amplitude values collected in the vector $\mathbf{A}_e$. In addition, $A_s(f_j, \zeta)$ is the simulated displacement amplitude obtained at f_j for the damping ratio ζ.

Table 3 provides the computed damping ratios with the associated MSE_s values. Such a table also gives the MSE values obtained by using the GBWM without additional viscous damping. In addition, Fig. 6a and b illustrate the experimental and simulated FRCs obtained without and with viscous damping corrections, respectively.

Such results suggest that the proposed mathematical model is particularly reliable to simulate the dynamic response in the middle-high base excitation range.

To sum up, we may note that the presented GBWM is extremely accurate in simulating the quasi-static behavior of the selected HWRI. Furthermore, if adopted in conjunction with a linear rate-dependent hysteresis model, it also achieves high accuracy in predicting the steady dynamic response of a rigid block supported by the HWRI.

5.2 Non-stationary response

We finally investigate the capability of the proposed mathematical model, adopting the GBWM with or without additional viscous damping, to simulate the dynamic response of the isolated rigid block when it is subjected to a base motion having a non-stationary nature, as it typically happens in real vibration isolation problems.

To this end, the rigid block mounted on the HWRI, illustrated in Fig. 3, was preliminary tested by imposing, at the base, four white noise signals having a frequency content in the range [5, 50] Hz and characterized by peak accelerations of 2.0 g, 2.8 g, 3.5 g and 5.8 g, respectively.

Subsequently, the GBWM, adopted with and without additional viscous damping corrections, is employed to simulate the time history of the mass relative displacement.

To investigate the accuracy of the numerical simulations, Table 4 presents the MSE_t values computed, for each applied white noise signal, as follows:

$$\mathrm{MSE}_t = \frac{100}{N\sigma_{\mathbf{u}_e}} \sum_{j=1}^{N} \left[u_{exp}(t_j) - u_s(t_j)\right]^2, \tag{35}$$

where $u_{exp}(t_j)$ and $u_s(t_j)$ indicate the experimental and simulated mass relative displacement at time t_j, respectively. In addition, $\mathbf{u}_e$ is a vector collecting the N experimental displacement values whereas $\sigma_{\mathbf{u}_e}$ represents its variance.

In addition, Table 5 shows the absolute values of the peak mass relative displacements recorded during the experimental tests as well as those provided by the GBWM employed with and without additional viscous damping.

We can observe that the GBWM gives the better estimates of the peak mass relative displacements for the white noise signals having peak accelerations equal to 2.8 g, 3.5 g and 5.8 g, respectively. On the contrary, the GBWM adopted with a damping ratio of 3.83% furnishes the peak mass relative displacement closer to the experimental value obtained for the white noise signal with peak base acceleration of 2.0 g.

Finally, Fig. 7 compares the time histories of the experimental and simulated mass relative displacements obtained for the white noise signals characterized by peak base accelerations of 2.0 g (Fig. 7a), 2.8

Table 3 MSE_s between experimental and simulated FRCs shown in Fig. 6

Base acceleration amplitude [g]	MSE_s [%]				
	GBWM	GBWM $+\zeta = 6.08\%$	GBWM $+\zeta = 3.83\%$	GBWM $+\zeta = 0.55\%$	GBWM $+\zeta = 1.53\%$
0.35	153.86	55.40	–	–	–
0.50	53.13	–	19.76	–	–
0.75	8.35	–	–	6.49	–
1.50	42.01	–	–	–	1.99

Table 4 MSE_t between experimental and simulated mass relative displacements obtained for the four White Noise (WN) signals

WN peak acceleration [g]	MSE_t [%]				
	GBWM	GBWM $+\zeta = 6.08\%$	GBWM $+\zeta = 3.83\%$	GBWM $+\zeta = 0.55\%$	GBWM $+\zeta = 1.53\%$
2.0	37.14	23.97	24.98	34.03	29.88
2.8	25.11	26.95	24.60	24.33	23.71
3.5	19.32	25.96	22.30	19.16	19.53
5.8	10.76	24.28	18.43	11.19	12.81

Table 5 Experimental and simulated peak mass relative displacements obtained for the four White Noise (WN) signals

WN peak accel. [g]	peak mass relative displacement [mm]					
	Experiment	GBWM	GBWM $+\zeta = 6.08\%$	GBWM $+\zeta = 3.83\%$	GBWM $+\zeta = 0.55\%$	GBWM $+\zeta = 1.53\%$
2.0	1.71	1.89	1.59	1.68	1.85	1.80
2.8	3.22	2.91	2.34	2.45	2.80	2.69
3.5	4.84	4.40	3.14	3.52	4.22	3.98
5.8	6.65	6.60	4.68	5.28	6.36	5.99

g (Fig. 7b), 3.5 g (Fig. 7c) and 5.8 g (Fig. 7d), respectively. To obtain such an excellent match, the simulations are performed by using the model that provides the lower MSE_t, as suggested by Table 4.

6 Conclusions

In this work, the generalized Bouc–Wen model, proposed by Carboni et al. [15], has been adopted to simulate the quasi-static response of a helical wire rope isolator characterized by asymmetric hysteresis loops. The comparison between experimental and simulated responses suggests an excellent model accuracy that leads to a mean square error of 0.21%.

In addition, the proposed model, calibrated on the basis of the quasi-static tests, has been employed to simulate both stationary and non-stationary dynamic responses of a rigid block mounted on the helical wire rope isolator.

It has been found that, when employed to reproduce frequency response curves obtained imposing base harmonic accelerations, such a model overestimates the experimental results because of the presence of additional rate-dependent hysteresis phenomena occurring during the dynamic tests. Consequently, to improve the accuracy of the numerical results, it is necessary to introduce an additional viscous damping dependent upon the excitation level.

On the other hand, when used to simulate the response of the isolated rigid block subjected to base white noise signals, the proposed model, adopted without additional viscous damping, displays a superior performance, particularly at the highest excitation level.

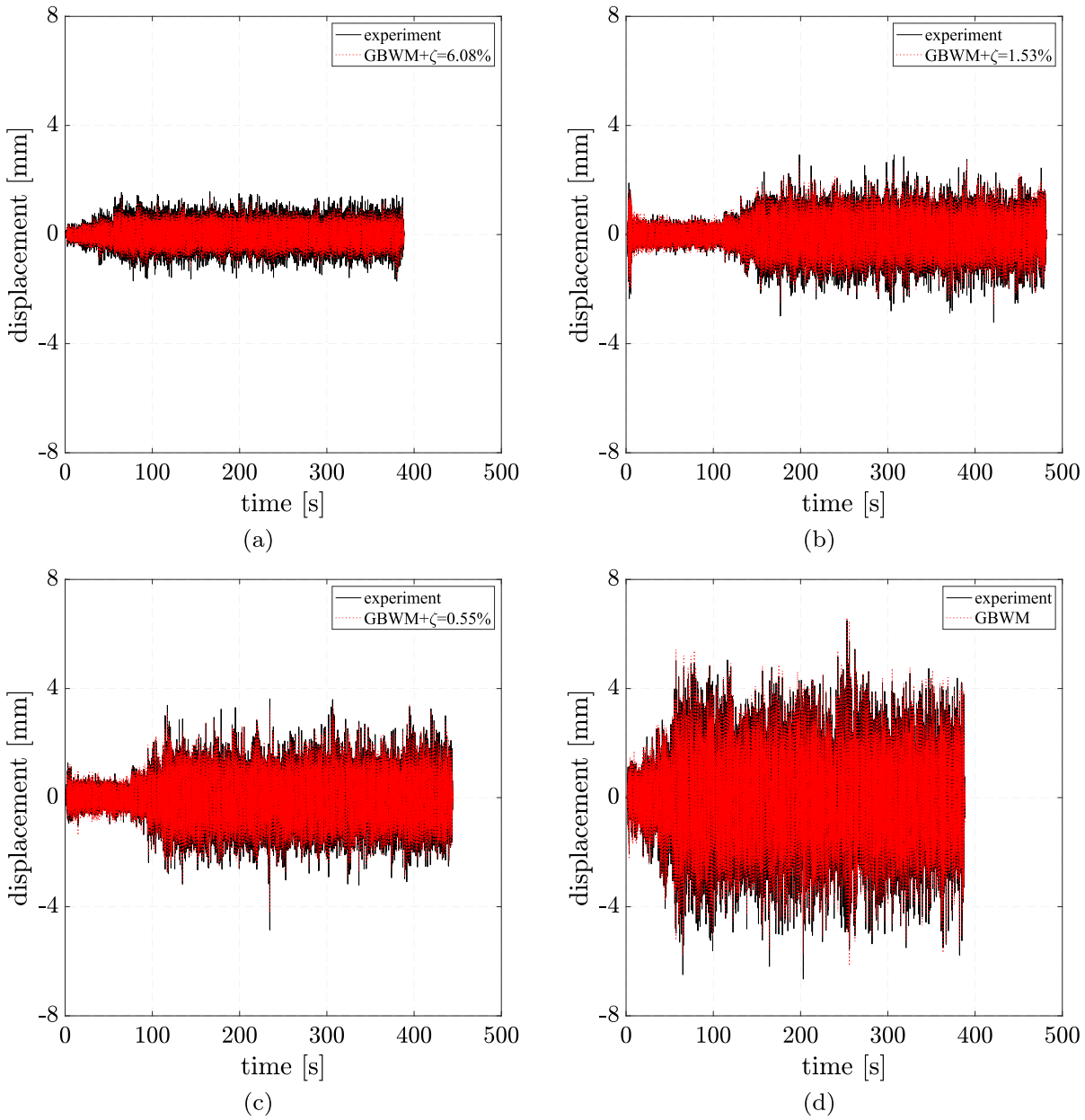

Fig. 7 Comparisons between experimental and simulated mass relative displacement histories obtained by imposing at the base a white noise signal having peak accelerations of **a** 2.0 g, **b** 2.8 g, **c** 3.5 g and **d** 5.8 g

It can be concluded that a quasi-static (dynamic) identification should be performed to simulate the behavior of mechanical systems equipped with helical wire rope isolators that work in non-stationary (or stationary) dynamic regimes. Based on the results obtained in this study, future investigations into the isolation capability of the HWRI are planned. Specifically, the isolation performance of a small rigid object will be studied both experimentally and numerically, employing the GBWM and a new experimental setup where several HWRIs will be placed in parallel. This investigation aligns with the authors' current research focus on the isolation of valuable art objects and sensitive equipment.

Acknowledgements The authors conducted this research in the framework of PRIN 2022 2022TH5HC2-Engineered Basements for Vibration Protection of Artworks and Strategic Sensitive Equipment (CUP Master: B53D23006440001), funded by the European Union—Next Generation EU (PI: B. Carboni, Substitute PI: N. Vaiana).

Author contributions RC Conceptualization, Software, Writing—original draft. NV Validation, Project administration, Funding acquisition, Supervision, Writing—review and editing. BC Conceptualization, Methodology, Software, Validation, Project administration, Funding acquisition, Supervision, Writing—review and editing.

Funding Open access funding provided by Università degli Studi di Roma La Sapienza within the CRUI-CARE Agreement. PRIN 2022 2022TH5HC2-Engineered Basements for Vibration Protection of Artworks and Strategic Sensitive Equipment (CUP Master: B53D23006440001), funded by the European Union—Next Generation EU (PI: B. Carboni, Substitute PI: N. Vaiana).

Data Availibility Statement Data will be made available on request.

Declarations

Conflict of interest The authors have no relevant financial or non-financial interests to disclose.

References

1. Al Jawhar, A.: Investigating wire rope isolator for seismic protection of floor-mounted equipment in a low-rise hospital building. PhD thesis, Howard University (2019)
2. Alessandri, S., Giannini, R., Paolacci, F., Amoretti, M., Freddo, A.: Seismic retrofitting of an HV circuit breaker using base isolation with wire ropes. Part 2: Shaking-table test validation. Eng. Struct. **98**, 263–274 (2015)
3. Alessandri, S., Giannini, R., Paolacci, F., Malena, M.: Seismic retrofitting of an HV circuit breaker using base isolation with wire ropes Part 1: preliminary tests and analyses. Eng. Struct. **98**, 251–262 (2015)
4. Aloisio, A., Alaggio, R., Köhler, J., Fragiacomo, M.: Extension of generalized Bouc–Wen hysteresis modeling of wood joints and structural systems. J. Eng. Mech. **146**(3), 04020001 (2020)
5. Antonelli, M., Carboni, B., Lacarbonara, W., Bernardini, D., Kalmár-Nagy, T.: Quantifying rate-dependence of a nonlinear hysteretic device. In: Nonlinear Dynamics of Structures, Systems and Devices: Proceedings of the First International Nonlinear Dynamics Conference (NODYCON 2019), vol. I, pp. 347–355. Springer (2020)
6. Baber, T.T., Noori, M.N.: Random vibration of degrading, pinching systems. J. Eng. Mech. **111**(8), 1010–1026 (1985)
7. Baber, T.T., Noori, M.N.: Modeling general hysteresis behavior and random vibration application. J. Vib. Acoust. **108**(4), 411–420 (1986)
8. Baber, T.T., Wen, Y.-K.: Random vibration of hysteretic, degrading systems. J. Eng. Mech. Div. **107**(6), 1069–1087 (1981)
9. Bouc, R.: Forced vibrations of mechanical systems with hysteresis. In: Proceedings of the Fourth Conference on Nonlinear Oscillations, Prague (1967)
10. Capuano, R., Vaiana, N., Carboni, B.: Experimental characterization and identification of the shear hysteretic behavior of a helical wire rope isolator. In: New Trends in Nonlinear Dynamics: Proceedings of the Third International Nonlinear Dynamics Conference (NODYCON 2023), vol. 3, pp. 49–57. Springer (2024)
11. Capuano, R., Vaiana, N., Pellecchia, D., Rosati, L.: A solution algorithm for a modified Bouc–Wen model capable of simulating cyclic softening and pinching phenomena. IFAC-PapersOnLine **55**(20), 319–324 (2022)
12. Capuano, R., Vaiana, N., Rosati, L.: Frequency-response curves for rate-independent hysteretic mechanical responses of complex shape. Nonlinear Dyn. (2024)
13. Carboni, B., Lacarbonara, W.: Nonlinear dynamic characterization of a new hysteretic device: experiments and computations. Nonlinear Dyn. **83**, 23–39 (2016)
14. Carboni, B., Lacarbonara, W.: Nonlinear vibration absorber with pinched hysteresis: theory and experiments. J. Eng. Mech. **142**(5), 04016023 (2016)
15. Carboni, B., Lacarbonara, W., Auricchio, F.: Hysteresis of multiconfiguration assemblies of nitinol and steel strands: experiments and phenomenological identification. J. Eng. Mech. **141**(3), 04014135 (2015)
16. Carboni, B., Lacarbonara, W., Brewick, P.T., Masri, S.F.: Dynamical response identification of a class of nonlinear hysteretic systems. J. Intell. Mater. Syst. Struct. **29**(13), 2795–2810 (2018)
17. De Canio, G.: Marble devices for the base isolation of the two Bronzes of Riace: a proposal for the David of Michelangelo. In: Proceedings of the 15th World Conference on Earthquake Engineering, pp. 24–28 (2012)
18. Demetriades, G.F., Constantinou, M.C., Reinhorn, A.M.: Study of wire rope systems for seismic protection of equipment in buildings. Eng. Struct. **15**(5), 321–334 (1993)
19. Destro Bisol, G., DeJong, M., Liberatore, D., Sorrentino, L.: Analysis of seismically-isolated two-block systems using a multi-rocking-body dynamic model. Comput. Aided Civ. Infrastruct. Eng. **38**(12), 1583–1604 (2023)

20. Destro Bisol, G., DeJong, M.J., Liberatore, D., Sorrentino, L.: Displacement-based design procedures for rigid block isolation. Earthq. Eng. Struct. Dyn. (2024)
21. Dimian, M., Andrei, P.: Noise-Driven Phenomena in Hysteretic Systems. Springer, Berlin (2017)
22. Dobson, S., Noori, M., Hou, Z., Dimentberg, M., Baber, T.: Modeling and random vibration analysis of SDOF systems with asymmetric hysteresis. Int. J. Non-Linear Mech. **32**(4), 669–680 (1997)
23. Foliente, G.C.: Hysteresis modeling of wood joints and structural systems. J. Struct. Eng. **121**(6), 1013–1022 (1995)
24. Ghayesh, M.H., Kazemirad, S., Darabi, M.A.: A general solution procedure for vibrations of systems with cubic nonlinearities and nonlinear/time-dependent internal boundary conditions. J. Sound Vib. **330**(22), 5382–5400 (2011)
25. Ghayesh, M.H., Kazemirad, S., Reid, T.: Nonlinear vibrations and stability of parametrically exited systems with cubic nonlinearities and internal boundary conditions: a general solution procedure. Appl. Math. Model. **36**(7), 3299–3311 (2012)
26. Kang, M.-S., Kim, J.-H., Kim, M.-H.: Experimental and numerical study on the vibration characteristics of an electric switchboard with wire rope isolators in naval ships. Ocean Eng. **283**, 115172 (2023)
27. Ko, J.M., Ni, Y.Q., Tian, Q.L.: Hysteretic behavior and emperical modeling of a wire-cable vibration isolator (1992)
28. Kumar, P.: Modal analysis of viscoelastic three-dimensional rotating beam with generic tip mass. Eur. J. Mech. A Solids **96**, 104734 (2022)
29. Kumar, P.: An analytical investigation of nonlinear response and stability characteristics of beam with three-dimensional tip mass. Meccanica **58**(10), 2051–2078 (2023)
30. Ledezma-Ramírez, D.F., Tapia-González, P.E.: On the effect of hysteresis in shock isolators for aeronautical applications. In: Proceedings of the Symposium of Aeronautical and Aerospace Processes, Materials and Industrial Applications: Presented at the XXV International Materials Research Congress–Cancun 2016 25, pp. 35–49. Springer (2018)
31. Marin-Artieda, C., Han, X.: Energy dissipation platforms based on wire rope isolators for the seismic protection of equipment. In: 16th World Conference on Earthquake Engineering (2017)
32. Moore, C., Svetlik, R., Williams, A.: Practical applications of cables and ropes in the ISS countermeasures system. In: 2017 IEEE Aerospace Conference, pp. 1–15. IEEE (2017)
33. Ni, Y., Ko, J.M., Wong, C.W., Zhan, S.: Modelling and identification of a wire-cable vibration isolator via a cyclic loading test, Part I: identification and response prediction. Proc. Inst. Mech. Eng. Part I J. Syst. Control Eng. **213**(3), 173–182 (1999)
34. Ni, Y.Q., Ko, J.M., Wong, C.W., Zhan, S.: Modelling and identification of a wire-cable vibration isolator via a cyclic loading test. Proc. Inst. Mech. Eng. Part I J. Syst. Control Eng. **213**(3), 163–172 (1999)
35. Paolacci, F., Giannini, R.: Study of the effectiveness of steel cable dampers for the seismic protection of electrical equipment. In: Proceedings of the 14th World Conference on Earthquake Engineering, pp. 12–17 (2008)
36. Pellecchia, D., Vaiana, N., Spizzuoco, M., Serino, G., Rosati, L.: Axial hysteretic behaviour of wire rope isolators: experiments and modelling. Mater. Des. **225**, 111436 (2023)
37. Quaranta, G., Lacarbonara, W., Masri, S.F.: A review on computational intelligence for identification of nonlinear dynamical systems. Nonlinear Dyn. **99**(2), 1709–1761 (2020)
38. Salvatore, A., Carboni, B., Chen, L.-Q., Lacarbonara, W.: Nonlinear dynamic response of a wire rope isolator: experiment, identification and validation. Eng. Struct. **238**, 112121 (2021)
39. Sireteanu, T., Giuclea, M., Mitu, A.M.: Identification of an extended Bouc-Wen model with application to seismic protection through hysteretic devices. Comput. Mech. **45**, 431–441 (2010)
40. Song, J., Der Kiureghian, A.: Generalized Bouc–Wen model for highly asymmetric hysteresis. J. Eng. Mech. **132**(6), 610–618 (2006)
41. Storn, R., Price, K.: Differential evolution—a simple and efficient heuristic for global optimization over continuous spaces. J. Global Optim. **11**, 341–359 (1997)
42. Vaiana, N., Capuano, R., Rosati, L.: Evaluation of path-dependent work and internal energy change for hysteretic mechanical systems. Mech. Syst. Signal Process. **186**, 109862 (2023)
43. Vaiana, N., Marmo, F., Sessa, S., Rosati, L.: Modeling of the hysteretic behavior of wire rope isolators using a novel rate-independent model. In: Nonlinear Dynamics of Structures, Systems and Devices: Proceedings of the First International Nonlinear Dynamics Conference (NODYCON 2019), vol. 1, pp. 309–317. Springer (2020)
44. Vaiana, N., Rosati, L.: Analytical and differential reformulations of the Vaiana–Rosati model for complex rate-independent mechanical hysteresis phenomena. Mech. Syst. Signal Process. **199**, 110448 (2023)
45. Vaiana, N., Rosati, L.: Classification and unified phenomenological modeling of complex uniaxial rate-independent hysteretic responses. Mech. Syst. Signal Process. **182**, 109539 (2023)
46. Vaiana, N., Spizzuoco, M., Serino, G.: Wire rope isolators for seismically base-isolated lightweight structures: experimental characterization and mathematical modeling. Eng. Struct. **140**, 498–514 (2017)
47. Wang, H.-X., Gong, X.-S., Pan, F., Dang, X.-J.: Experimental investigations on the dynamic behaviour of O-type wire-cable vibration isolators. Shock Vib. **2015** (2015)
48. Wang, T., Noori, M., Altabey, W.A., Wu, Z., Ghiasi, R., Kuok, S.-C., Silik, A., Farhan, N.S.D., Sarhosis, V., Farsangi, E.N.: From model-driven to data-driven: a review of hysteresis modeling in structural and mechanical systems. Mech. Syst. Signal Process. **204**, 110785 (2023)
49. Wen, Y.-K.: Method for random vibration of hysteretic systems. J .Eng. Mech. Div. **102**(2), 249–263 (1976)
50. Zhang, Y.-W., Wang, Z.-J., Cao, M., Song, X.-Y., Zang, J., Lacarbonara, W., Chen, L.-Q.: Vibration control of composite laminate via NiTiNOL-steel wire ropes: modeling, analysis, and experiment. Mech. Syst. Signal Process. **204**, 110775 (2023)